Available online at www.sciencedirect.com

ScienceDirect

Energy Procedia 45 (2014) 528 – 537

Energy Procedia

68th Conference of the Italian Thermal Machines Engineering Association, ATI2013

High-order discontinuous Galerkin solutions of internal low-Mach number turbulent flows

V. Covello[a,*], A. Nigro[a], C. De Bartolo[a], G. Florio[a]

[a]*University of Calabria-Department of Mechanical, Energetic and Management Engineering, Ponte P. Bucci cubo 44/C, Rende (CS) 87036, Italy*

Abstract

In this work we apply the high-order Discontinuous Galerkin (DG) finite element method to internal low-Mach number turbulent flows. The method here presented is designed to improve the performance of the solution in the incompressible limit using an implicit scheme for the temporal integration of the compressible Reynolds Averaged Navier Stokes (RANS) equations . The performance of the scheme is demonstrated by solving a well-known test-case consisting of an abrupt axisymmetric expansion using various degrees of polynomial approximation. Computations with k-ω model are performed to assess the modelling capabilities, with high-order accurate DG discretizations of the RANS equations, in presence of non-equilibrium flow conditions.

Selection and peer-review under responsibility of ATI NAZIONALE

Keywords: Computational Fluid Dynamics, Discontinuous Galerkin finite element method, RANS equations, $k-\omega$ turbulence model, internal flows, abrupt expansion.

1. Introduction

The design and research activities in the field of turbomachinery and internal combustion engines are currently mainly focused on achieving high level of environmental compatibility, both in terms of reduced air pollutant emissions and energy consumptions. In this context the considerable advances in algorithms development and the huge increase of the computer power have made Computational Fluid Dynamics (CFD) a key discipline for industrial growth during the last two decades. The flow fields inside a turbomachinery or an Internal Combustion Engine (ICE) system greatly affect the performance and the level of exhaust emissions, then a more accurate prediction of their complex physics phenomena could provide considerable benefits in order to reduce time and costs of the industrial production cycles. The turbulent flow prediction by standard industrial codes is currently mainly based on the numerical solution of Reynolds Averaged Navier Stokes Equations (RANS) by means of formally second-order accurate finite volume schemes, due to their robustness and their favourable computational cost-accuracy ratio. On the other hand the numerical accuracy provided by these low-order schemes is often inadequate to meet the increasing demand of advanced industrial sectors to improve CFD-aided design and analysis procedures. Low-order schemes, in

* V. Covello Tel.: +39 0984 494942 ; fax: +39 0984 494673
E-mail address: vanessa.covello@unical.it

1876-6102
Selection and peer-review under responsibility of ATI NAZIONALE
doi:10.1016/j.egypro.2014.01.057

fact, fail to properly reproduce the fluid dynamic behaviour of complex turbulent flows, especially in the presence of non-equilibrium phenomena, high streamlines curvature or strong three-dimensional effects.

In recent years several high-order methods have been emerging as practical tools to go beyond the second-order accuracy of standard finite volume discretizations and among them the Discontinuous Galerkin (DG) finite element method, has received increasing attention in computational fluid dynamics due to its many attractive features [1–6]. The DG method is an innovative strategy that combines two key ideas which are at the basis of the finite volume and of the finite element methods, approximating the solution in each element by piecewise polynomial functions with no global continuity requirement at element interfaces. Like continuous finite element methods, the DG method can increase the accuracy raising the degree of polynomial approximation inside each element, whereas the discontinuous approximation at element interfaces allows the method to employ upwind discretizations of interface fluxes, like in high-resolution finite volume methods. The lake of global continuity allows the treatment of each element as a separate entity that communicates with the adjacent elements only through the numerical fluxes. This feature of the method gives a good capability of parallelization. Furthermore, its compact formulation can be applied close to the boundary without any special treatment, thus increasing the robustness and the accuracy of every boundary conditions. Finally, the dispersion and dissipative properties of the method are excellent. These latter aspects (boundary treatment, dispersion and dissipation) are crucial in order to deal with turbulent flows in complex geometries typical of ICE and turbomachinery applications. Up to now the major implementation efforts in order to apply the DG method in CFD were mainly concentrated on resolution of external aerodynamics problems. The performances already proved by the DG scheme for external flows are expected also for internal flows.

The aim of this work is to analyse the effectiveness of the method in the context of internal low-Mach number turbulent flows, by solving a well-known test-case [7] consisting of an abrupt axisymmetric expansion using various degrees of polynomial approximation. Computations with k-ω turbulence model are performed and compared to the experimental data in order to assess the modelling capabilities, with high-order accurate DG discretizations of the RANS equations, in presence of non-equilibrium flow conditions. This is a first step of a study that aims to assess the potential of a high-order DG discretization coupled with high-level turbulence modelling capabilities when dealing with internal turbulent flows of industrial interest. The paper is organized as follows: section 2 presents the coupled set of RANS and $k-\omega$ equations, section 3 describes the main features of the DG discretization and section 4 refers to the implicit time integration. In section 5 the results of several numerical tests are discussed and compared with experimental data and section 6 contains the conclusions.

2. Governing equations

Here we consider the coupled set of RANS and $k-\omega$ equations in axisymmetric coordinates [8] since they correctly model the physics of the test-case investigated. The two-dimensional RANS and $k-\omega$ equations for compressible flows with no-swirl component can be written in conservative form as

$$\frac{\partial}{\partial t}(\rho r)+\frac{\partial}{\partial z}(\rho r v_z)+\frac{\partial}{\partial r}(\rho r v_r)=0, \tag{1}$$

$$\frac{\partial}{\partial t}(\rho r e_t)+\frac{\partial}{\partial z}(\rho r h_t v_z)+\frac{\partial}{\partial r}(\rho r h_t v_r)=A+B-rP+\beta^*\rho r\bar{k}e^{\tilde{\omega}_r}, \tag{2}$$

$$\frac{\partial}{\partial t}(\rho r v_z)+\frac{\partial}{\partial z}\left[r\left(p+\rho v_z^2\right)\right]+\frac{\partial}{\partial r}(\rho r v_z v_r)=\frac{\partial}{\partial z}(r\hat{\tau}_{zz})+\frac{\partial}{\partial r}(r\hat{\tau}_{zr}), \tag{3}$$

$$\frac{\partial}{\partial t}(\rho r v_r)+\frac{\partial}{\partial z}(\rho r v_z v_r)+\frac{\partial}{\partial r}\left[r\left(p+\rho v_r^2\right)\right]-p=\frac{\partial}{\partial z}(r\hat{\tau}_{zr})+\frac{\partial}{\partial r}(r\hat{\tau}_{rr}), \tag{4}$$

$$\frac{\partial}{\partial t}(\rho r k)+\frac{\partial}{\partial z}(\rho r v_z k)+\frac{\partial}{\partial r}(\rho r v_z k)=\frac{\partial}{\partial z}\left(\bar{\mu}_k r\frac{\partial k}{\partial z}\right)+\frac{\partial}{\partial r}\left(\bar{\mu}_k r\frac{\partial k}{\partial r}\right)+rP-\beta^*\rho r\bar{k}e^{\tilde{\omega}_r}, \tag{5}$$

$$\frac{\partial}{\partial t}(\rho r\tilde{\omega})+\frac{\partial}{\partial z}(\rho r v_z\tilde{\omega})+\frac{\partial}{\partial r}(\rho r v_r\tilde{\omega})=\frac{\partial}{\partial z}\left(\bar{\mu}_\omega r\frac{\partial\tilde{\omega}}{\partial z}\right)+\frac{\partial}{\partial r}\left(\bar{\mu}_\omega r\frac{\partial\tilde{\omega}}{\partial r}\right)+\frac{\alpha r\tilde{\omega}}{\bar{k}}P-\beta\rho r e^{\tilde{\omega}_r}. \tag{6}$$

in which ρ , p , $\mathbf{v} = (v_z, v_r)$, e_t , $h_t = e_t + p/\rho$ denote the density, pressure, velocity, total internal energy and total enthalpy of the mean motion, respectively. For polytropic ideal gases the pressure is given by

$$p = (\gamma - 1)\rho\left(e_t - \frac{v_z^2}{2} - \frac{v_r^2}{2}\right),$$

where γ is the constant ratio of specific heats. The term A on the right-hand side of Eq. (2) denotes the divergence of the work of total stresses $\nabla \cdot (r\hat{\tau}\mathbf{v})$ and B the divergence of total heat flux vector $\nabla \cdot (r\mathbf{q})$. Specifically,

$$A = r\frac{\partial}{\partial z}\left(\hat{\tau}_{zz}v_z + \hat{\tau}_{zr}v_r\right) + \frac{\partial}{\partial r}\left(r\hat{\tau}_{zr}v_z + r\hat{\tau}_{rr}v_r\right),$$

$$B = -r\frac{\partial q_z}{\partial z} - \frac{\partial (rq_r)}{\partial r},$$

where the turbulent stress tensor components are defined as

$$\tau_{zz} = 2\bar{\mu_t}\left(\frac{\partial v_z}{\partial z} - \frac{1}{3}\nabla \cdot \mathbf{v}\right) - \frac{2}{3}\rho k,$$

$$\tau_{rr} = 2\bar{\mu_t}\left(\frac{\partial v_r}{\partial r} - \frac{1}{3}\nabla \cdot \mathbf{v}\right) - \frac{2}{3}\rho k,$$

$$\tau_{zr} = \bar{\mu_t}\left(\frac{\partial v_z}{\partial r} + \frac{\partial v_r}{\partial z}\right),$$

and the total stresses $\hat{\tau}$ are given by the sum of turbulent and viscous stresses:

$$\hat{\boldsymbol{\tau}} = \boldsymbol{\tau} + \frac{\mu}{\mu_t}\left(\boldsymbol{\tau} + \frac{2}{3}\rho k\mathbf{I}\right).$$

Moreover the heat flux components are given by

$$q_z = \lambda\frac{\partial h}{\partial z}, \qquad q_r = \lambda\frac{\partial h}{\partial r},$$

in which λ indicates the gas conductivity. It is worth pointing out the presence of a source term in Eq. (2) related to the fact that the turbulent kinetic energy is not included in total internal energy and in total enthalpy. The production term that models the energy exchange between mean and turbulent field can be written as

$$P = \bar{\mu_t}\left\{2\left[\left(\frac{\partial v_z}{\partial z}\right)^2 + \left(\frac{\partial v_r}{\partial r}\right)^2 + \left(\frac{v_r}{r}\right)^2\right] + \left(\frac{\partial v_r}{\partial z} + \frac{\partial v_z}{\partial r}\right)^2 - \frac{2}{3}\left(\nabla \cdot \mathbf{v}\right)^2\right\} - \frac{2}{3}\rho k\nabla \cdot \mathbf{v},$$

$$\nabla \cdot \mathbf{v} = \frac{\partial v_z}{\partial z} + \frac{\partial v_r}{\partial r} + \frac{v_r}{r}.$$

The turbulence model adopted is the $k-\omega$ Wilcox high-Reynolds number turbulence model [9], where the turbulent eddy viscosity and the effective viscosity coefficients of the turbulence equations are as follows:

$$\mu_t = \frac{\alpha^*\rho k}{\omega}, \qquad \mu_k = \mu + \sigma^*\mu_t, \qquad \mu_\omega = \mu + \sigma\mu_t, \tag{7}$$

where α, α^*, β, β^*, σ, and σ^* stand for the closure coefficients. Following the approach described in [10,11], the model employs the variable $\tilde{\omega} = ln(\omega)$ instead of ω to guarantee the positivity of ω and to obtain a smoother near wall distribution. Moreover, the variables k and $\tilde{\omega}$ are limited from below by

$$\overline{k} = max(k, 0), \qquad \widetilde{\omega_r} = max(\tilde{\omega_{r0}}, \tilde{\omega}),$$

where $\tilde{\omega_{r0}}$ defines the lower bound on $\widetilde{\omega}$ that ensures the positivity of normal turbulent stresses and the fulfillment of the Schwarz inequality for shear turbulent stresses. The turbulent eddy viscosity and effective eddy viscosity are then computed by the following expressions:

$$\bar{\mu}_t = \alpha^*\rho\overline{k}e^{-\widetilde{\omega}_r}, \qquad \bar{\mu_k} = \mu + \sigma^*\bar{\mu}_t, \qquad \bar{\mu_\omega} = \mu + \sigma\bar{\mu}_t.$$

3. Discontinuous Galerkin discretization

The RANS and $k-\omega$ turbulence model Eqs. (1-6) can be written in compact form as

$$\frac{\partial (r\mathbf{u})}{\partial t} + \nabla \cdot (r\mathbf{F}_c(\mathbf{u})) + \nabla \cdot (r\mathbf{F}_v(\mathbf{u}, \nabla \mathbf{u})) + r\mathbf{s}(\mathbf{u}, \nabla \mathbf{u}) = 0, \tag{8}$$

where $\mathbf{u} \in \mathbb{R}^M$ denotes the vector of the M conservative variables, $\mathbf{s} \in \mathbb{R}^M$ the sum of turbulent and axisymmetric source term vectors, $\mathbf{F}_c, \mathbf{F}_v \in \mathbb{R}^M \otimes \mathbb{R}^N$ denote the inviscid and viscous flux functions, respectively, and N is the space dimension.

In order to construct the DG space discretization of the coupled set of RANS and $k-\omega$ equations, we define $\mathbf{V}_h$ to be the space of discontinuous vector-valued polynomials of degree n, on a subdivision τ_h of the domain Ω into non-overlapping elements K such as $\Omega_h = \bigcup_{K \in \tau_h} K$. Thus, the solution and test functions space is defined by

$$\mathbf{V}_h = \{\mathbf{v}_h \in L^2(\Omega_h) : \mathbf{v}_h|_K \in P_n(K) \, \forall K \in \tau_h\},$$

where $P_n(K)$ is the space of polynomial functions of degree at most n in the element K. Ω_h is the discrete approximation of the domain, $\partial\Omega_h$ the boundary, Γ_h^0 the set of internal edges and $\Gamma_h = \Gamma_h^0 \bigcup \partial\Omega_h$.

The DG formulation of the Eq. (8) is seeking for $\mathbf{u}_h \in \mathbf{V}_h$ such as, for an arbitrary test function $\mathbf{v}_h \in \mathbf{V}_h$, the following equation is satisfied:

$$\begin{aligned}
&\int_{\Omega_h} \mathbf{v}_h \cdot \frac{\partial \mathbf{u}_h}{\partial t} r d\mathbf{x} - \int_{\Omega_h} \boldsymbol{\nabla} \mathbf{v}_h : (\mathbf{F}_c(\mathbf{u}_h) - \mathbf{F}_v(\mathbf{u}_h, \boldsymbol{\nabla}\mathbf{u}_h + \mathcal{R}([\![\mathbf{u}_h]\!]_0))) \, r d\mathbf{x} \\
&+ \int_{\Gamma_h^0} \left(\mathbf{v}_h^- - \mathbf{v}_h^+\right) \cdot \mathbf{H}\left(\mathbf{u}_h^+, \mathbf{u}_h^-, \mathbf{n}\right) r d\sigma - \int_{\Gamma_h^0} [\![\mathbf{v}_h]\!] : \{\mathbf{F}_v(\mathbf{u}_h, \boldsymbol{\nabla}\mathbf{u}_h + \eta_e \mathcal{R}_e([\![\mathbf{u}_h]\!]_0)\} \, r d\sigma \\
&+ \int_{\partial\Omega_h} (\mathbf{v}_h \otimes \mathbf{n}) : \left(\mathbf{H}\left(\mathbf{u}_h^+, \mathbf{u}_h^b, \mathbf{n}\right) - \mathbf{F}_v(\mathbf{u}_h, \boldsymbol{\nabla}\mathbf{u}_h + \eta_e \mathcal{R}_e([\![\mathbf{u}_h]\!]_0))_b\right) r d\sigma = 0
\end{aligned} \tag{9}$$

Such discretization is based on the BR2 scheme for the approximation of the viscous part [10,12]. η_e is called "penalty" parameter and its lower bound is established as the number of neighbours of the generic element K, to guarantee the stability of the method. $\mathcal{R}_e([\![\mathbf{u}_h]\!])$ and $\mathcal{R}([\![\mathbf{u}_h]\!]_0)$ stand respectively for the local and global lifting operators accounting in the gradient of the diffusive fluxes for the jumps in $\mathbf{u}_h$ occurring at the element interfaces, defined as:

$$[\![\mathbf{u}_h]\!]_0 = \begin{cases} [\![\mathbf{u}_h]\!] & \text{on} \quad \Gamma_h{}^0 \\ \mathbf{u}_h \otimes \mathbf{n} & \text{on} \quad \partial\Omega_h \end{cases}$$

in whitch the jump $[\![\cdot]\!]$ operator is

$$[\![\mathbf{u}_h]\!] = \mathbf{u}_h^+ \otimes \mathbf{n}^+ + \mathbf{u}_h^- \otimes \mathbf{n}^-,$$

and the trace operator $\{(\cdot)\}$ denotes the average between the right $(\cdot)^+$ and the left $(\cdot)^-$ state. Furthermore, $\mathbf{H}\left(\mathbf{u}_h^+, \mathbf{u}_h^-, \mathbf{n}\right)$ and $\mathbf{H}\left(\mathbf{u}_h^+, \mathbf{u}_h^b, \mathbf{n}\right)$ are the numerical flux functions at the interior and boundary faces, respectively. Any numerical flux functions commonly considered in the finite volume method can be used for the evaluation of the inviscid part of the numerical fluxes. In this paper we employ the Godunov flux, i.e. the physical flux of the exact solution of a planar Riemann problem in the direction normal to the boundary.

4. Time integration

The DG space discretization, Eq. (9), results in the following system of ordinary differential equations in time:

$$\mathbf{M}\frac{d\mathbf{U}}{dt} + \mathbf{R}(\mathbf{U}) = 0, \tag{10}$$

where $\mathbf{M}$ denotes the global mass matrix, and $\mathbf{U}$ and $\mathbf{R}$ are the global vectors of degrees of freedom (dofs) and of residuals, respectively. As in [13], the implicit time discretization is used to efficiently compute low-Mach number

flows without time-derivative preconditioning. Hence, the Eq. (10) is discretized in time using the implicit backward Euler scheme:

$$\left[\frac{\mathbf{M}}{\Delta t}+\frac{\partial \mathbf{R}^{n}}{\partial \mathbf{U}}\right]\Delta \mathbf{U}^{n}=-\mathbf{R}^{n}, \tag{11}$$

where $\Delta \mathbf{U}^{n}=\mathbf{U}^{n+1}-\mathbf{U}^{n}$, $\frac{\partial \mathbf{R}^{n}}{\partial \mathbf{U}}$ is the Jacobian matrix of the DG space discretization and $\left[\frac{\mathbf{M}}{\Delta t}+\frac{\partial \mathbf{R}^{n}}{\partial \mathbf{U}}\right]$ denotes the global system matrix. The matrix $\left[\frac{\mathbf{M}}{\Delta t}+\frac{\partial \mathbf{R}^{n}}{\partial \mathbf{U}}\right]$ can be regarded as an $N_K \times N_K$ block sparse matrix where N_K is the number of elements in τ_h and the rank of each block is $M \times N_{dof}^{K}$, where N_{dof}^{K} is the number of dofs for each of the M conservative variables in the generic element K. The Jacobian matrix of the DG discretization has been computed analytically without any approximation and, using very large time steps, the method can therefore achieve quadratic convergence in the computation of steady state solutions. In the limit $\Delta t \rightarrow \infty$ Eq. (11) is in reality identical to one iteration of the Newton method applied to the steady discrete problem. Finally, we underline that, to solve Eq. (11), we have used the restarted GMRES algorithm with ILU(0) available in the PETSc library [14].

5. Numerical Results

5.1. Test-case descritpion

The test-case analysed [7] is an axisymmetric sudden expansion with an expansion ratio approximately of 0.5. The flow conditions are without swirl with a Reynolds number of $Re = 30000$, based on the diameter and on the flow quantities at the inlet section of the duct. This test-case aims at evaluating the potential of the DG approach for internal turbulent flows in the presence of flow separation that occurs in many industrial applications such as the intake systems of ICE, through nacelle in a crosswind and in many others applications.

5.2. Boundary conditions

At the inlet, the velocity profile has been taken from the experimental measurements and then converted into an entropy profile by assuming a constant static pressure and with a given stagnation enthalpy so that the implementation of the inlet boundary condition has been carried out in the manner described in [15]. Moreover, the values of turbulence intensity, I_t, and turbulent viscosity ratio, $\frac{\mu_t}{\mu}$, assigned at the inlet are $I_t = 4\%$ and $\frac{\mu_t}{\mu} = 50$, respectively. Conversely, at the outlet boundary, only the pressure has been specified in order to obtain a Mach number of 0.05 at the inlet, whereas entropy, total enthalpy and flow angles have been extrapolated from the interior. At the wall a zero heat flux (adiabatic) no-slip boundary condition has been imposed. The wall boundary condition $\hat{\omega}_w$ has been set as proposed by Menter in [16]. The prescribed smooth wall value ω_w is related to the first cell-height $2y_1$ according to the relation

$$\omega_w = \frac{6\nu}{\beta\,(\alpha_M y_1)^2},$$

where $\alpha_M = \frac{1}{\sqrt{10}}$ and β is a real number depending on the polynomial degree.

5.3. Test-case setup

Although the experiments have been carried out using water, the computations have been performed with a compressible DG solver at the Mach number of 0.05 and the same Reynolds number of the experiment. The low compressibility of the present flow conditions has a very small impact on the accuracy of the numerical results. The computations have been performed, starting from an uniform flow field, with a sequence of polynomial approximations up to the sixth order of accuracy. The computational domain starts two diameters D upstream the abrupt expansion and it ends fifteen diameters downstream. Owing to the axisymmetric nature of the problem, we use a two-dimensional grid composed by 2400 quadrangular cells (Fig.1). The origin of the $z - axis\,(r = 0)$ is located at the inflow of the duct and the change of section is placed at $z = 0.1$. The diameters upstream and downstream of the

expansion are $D = 0.05078m$ and $D_2 = 0.0985m$, respectively. In Fig. 1 the considered measurement stations based on the ratio z/D are shown.

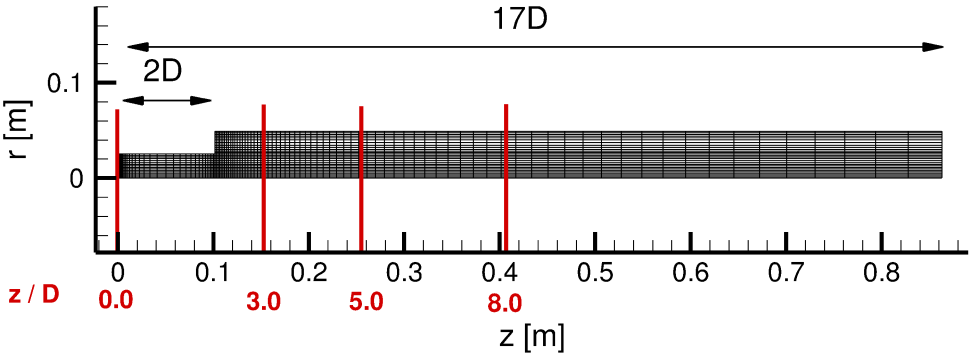

Fig. 1: Computational grid for the abrupt axisymmetric expansion test-case, including measurement stations.

To assess the performances of the proposed DG method in terms of accuracy we perform both a qualitative and quantitative analysis of the numerical results. For the former analysis we present the contour plots of pressure in the channel and the streamtraces at the recirculation region close to the abrupt expansion, for the latter we compare the numerical axial velocity profiles with the Dellenback's experimental data. Finally, the skin friction C_f distribution along the wall is shown to determine the separation point.

5.4. Accuracy of the results

In this section we present the results obtained by the DG code and their validation against the experimental data. Fig. 2 shows the behaviour of the y^+ for the first cell-centroid y_1 at the sections given in Fig. 1 for different polynomial degrees. The distance of the first grid line parallel to the wall of the duct is equal to $2y_1 = 0.0015$. As expected the highest y^+ values have been computed at the inlet where a polynomial approximation dependency of y^+ is evident. Conversely, after the sudden expansion, the y^+ values reduce almost independently of the spatial discretization.

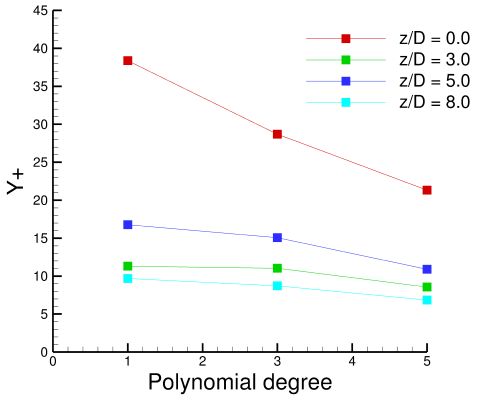

Fig. 2: y^+ values for the first cell-centroid y_1 as a function of different polynomial degrees at the considered measurement stations.

The plots in Fig. 3 show the pressure contours for P_1, P_3 and P_5 elements. Such plots point out qualitatively the prediction capability of the DG method for different polynomial approximations and how an increase in the polynomial degree leads to a significant improvement in the characterization of the pressure field.

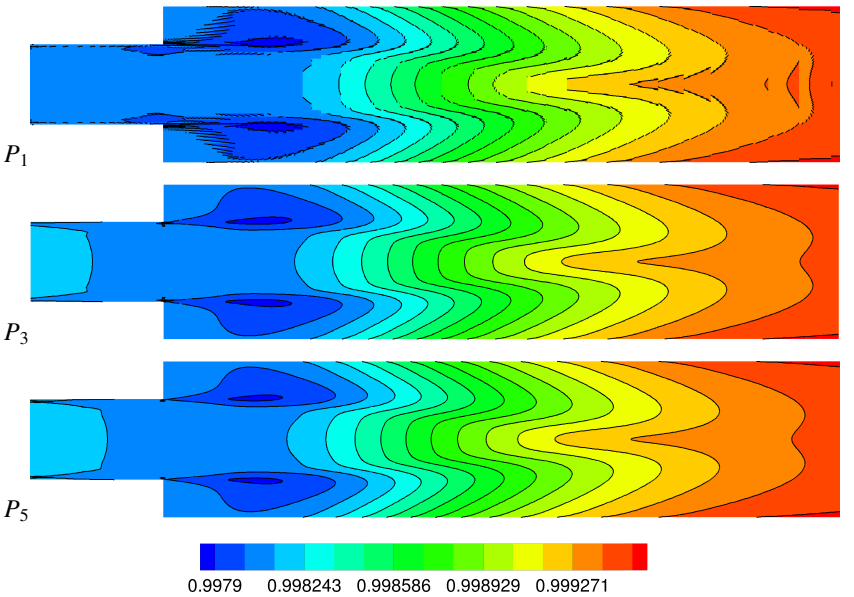

Fig. 3: Contours of pressure obtained using P_1 (top row), P_3 (middle row) and P_5 (bottom row) elements.

The effects of a high-order discretization on the solution accuracy are more evident in Fig. 4 that shows the streamlines close to the dump for different polynomial degrees. Notice that the lower order P_1 solution fails to capture the presence of recirculating regions close to the corner of the wall, whereas the P_3 solution predicts the presence of two contra-rotating vortices. Moreover, a further increase in the polynomial degree, from P_3 to P_5, only slightly affects the streamlines pattern.

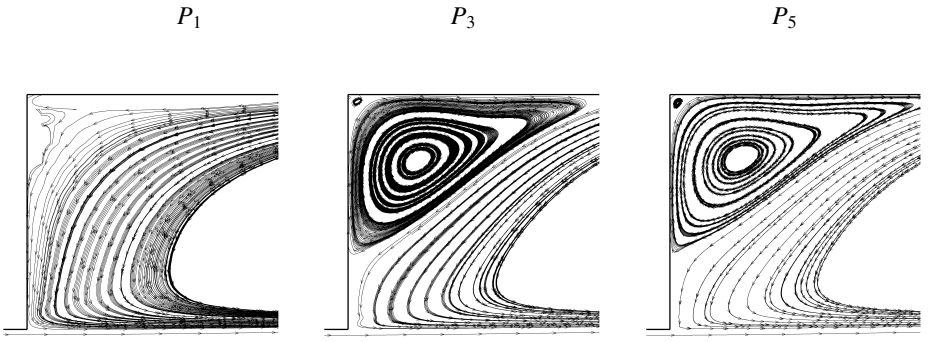

Fig. 4: Snapshots of streamtraces close to the corner of the wall, for P_1 (left column), P_3 (middle column) and P_5 (right column) elements.

The quantitative assessment of the numerical results has been carried out by comparing the axial velocities measured inside the duct along the sections indicated in Fig. 1. The numerical and experimental comparison is reported in Fig. 5 as a function of the radial distance from the axis, for different polynomial degrees.

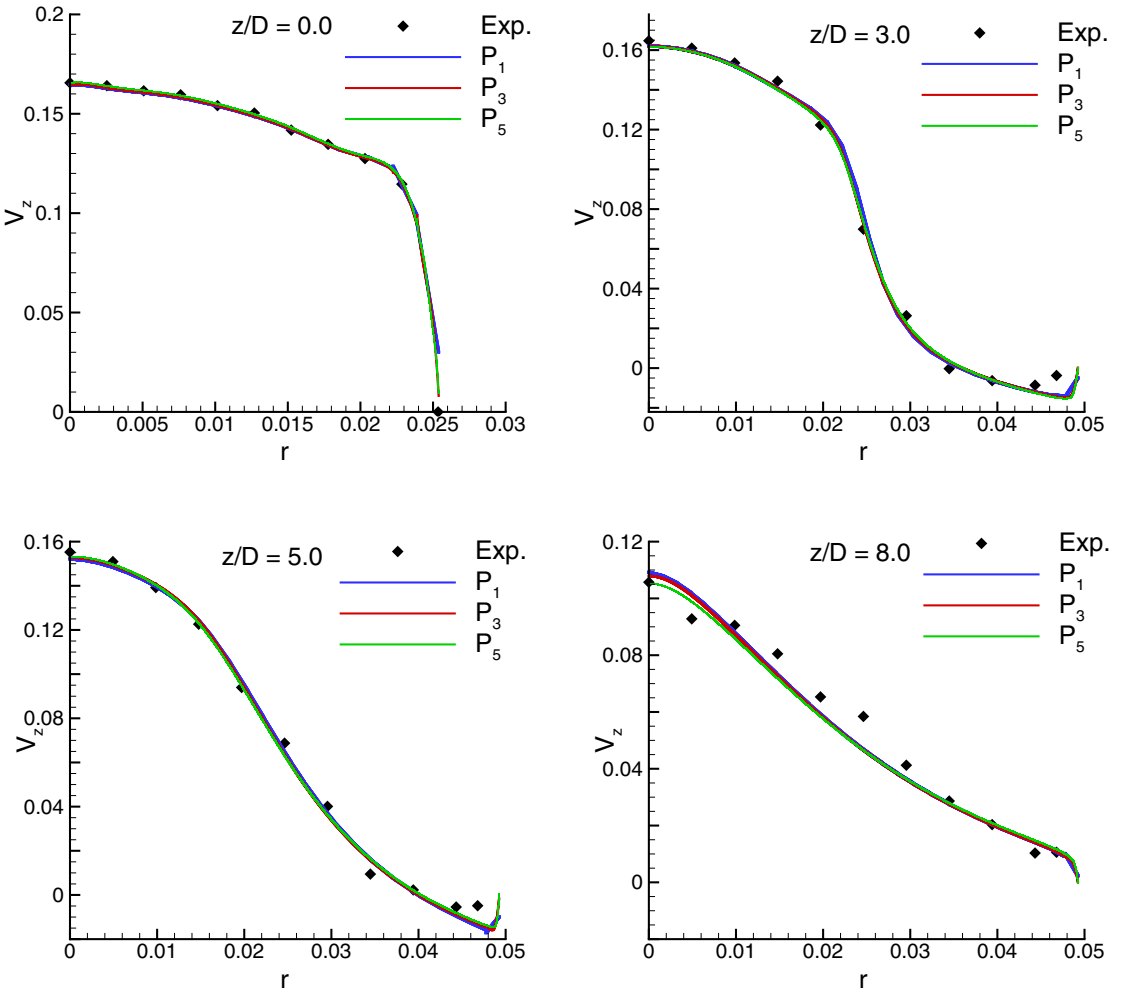

Fig. 5: DG axial velocity profiles compared with the experimental data at the considered measurement stations: $z/D = 0.0$ and $z/D = 3.0$ (top row), $z/D = 5.0$ and $z/D = 8.0$ (bottom row).

We observe that even using P_1 elements the numerical profiles are in good agreement with the experimental ones. Nevertheless, while the higher accuracy only marginally affects the computation of the axial velocity at certain distance from the axis, the higher degrees of approximation allow a more accurate prediction of the flow close to the axis and to the wall, as shown in Fig. 6.

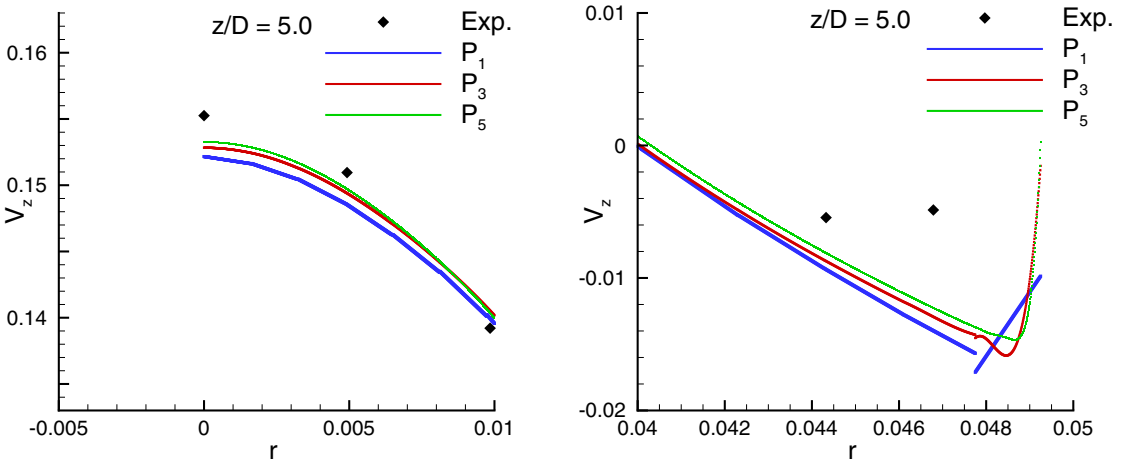

Fig. 6: DG axial velocity profiles compared with the experimental data at $z/D = 5.0$, close-up near the axis (left column) and the wall (right column).

In Fig. 7 the skin friction C_f distribution along the wall of the duct is shown for elements ranging from P_1 to P_5. The plot shows that P_1 and P_2 solutions suffer from a lack of accuracy, whereas the higher order approximations converge towards the same solution. This result suggests that the higher order solutions resolve boundary layers and recirculating regions more accurately. Finally, the reattachment length, approximately equal to $0.36m$, is almost independent on the order of accuracy and slightly overestimated respect to the experimental value of $0.3218m$.

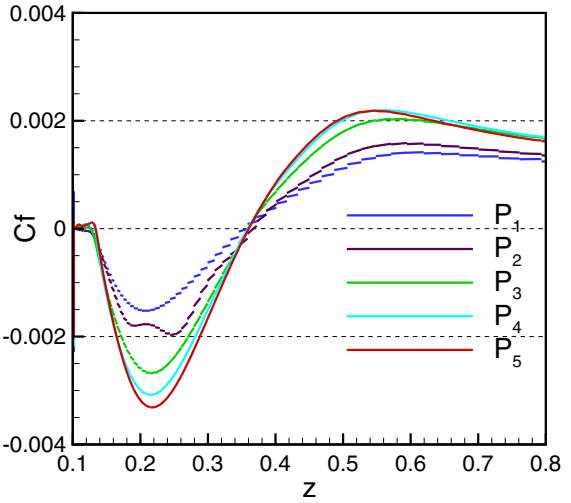

Fig. 7: Skin friction coefficient C_f along the wall of the duct, for P_1, P_2, P_3, P_4 and P_5 elements.

6. Conclusions

In this article we have presented high-order accurate Discontinuous Galerkin solutions of the coupled set of RANS and k-ω equations for an axisymmetric turbulent flow inside a channel with an abrupt expansion. Computations have been carried out using up to P_5 polynomial approximations (sixth-order accurate space discretization). The semi-discrete system of equations has been solved by means of the backward Euler scheme. Numerical solutions have been compared with experimental data to assess the predictive capability of the proposed DG scheme. Both axial velocity profiles along different sections inside the duct and the reattachment length have been considered to verify the accuracy of the computed flow fields. The comparisons between numerical and experimental data were satisfactory in both aspects. The simulations were also important to highlight that the higher-order accurate solutions are characterized by boundary layer and recirculation regions better resolved than those of lower order. These results point out the significant potential of the proposed DG scheme in computing high-order solutions of internal turbulent flows in complex geometries.

References

[1] Cockburn B, Hou S, Shu CW. The RungeKutta local projection discontinuous Galerkin finite element method for conservation laws IV: the multidimensional case. Math Comput, Vol. 54; 1990. p. 454-581.
[2] Cockburn B, Shu CW. The RungeKutta discontinuous Galerkin finite element method for conservation laws V: multidimensional systems. J Comput Phys, Vol.141; 1998. p. 199-224.
[3] Cockburn B, Hou S, Shu C-W. The RungeKutta local projection discontinuous Galerkin finite element method for conservation laws IV: the multidimensional case. Math Comput 1990;54:454-581.
[4] Cockburn B, Shu C-W. The RungeKutta discontinuous Galerkin finite element method for conservation laws V: multidimensional systems. J Comput Phys 1998;141:199-224.
[5] Hartmann R, Held L, Leicht T. Adjoint-based error estimation and adaptive mesh refinement for the rans and $k-\omega$ turbulence model equations. J Comput Phys. Vol. 230(11), 2011. p. 4268-4284.
[6] Chou CS, Shu CW. High order residual distribution conservative finite difference WENO schemes for convection-diffusion steady state problems on non-smooth meshes. J Comput Phys Vol. 224; 2006. p. 992-1020.
[7] Dellenback PA, Metzger DE, Neitzel GP. Measurements in Turbulent Swirling Flow Through an Abrupt Axisymmetric Expansion. AIAA journal, Vol. 26, No. 6; 1988.
[8] Bassi F, Cecchi F, Franchina N, Rebay S, Savini M. High-order discontinuous Galerkin computation of axisymmetric transonic flows in safety relief valves. Computers & Fluids, 49; 2011. p. 203-213.
[9] Wilcox DC. Turbulence modelling for CFD. La Canada, CA 91011, USA: DCW industries Inc.; 1993.
[10] Bassi F, Crivellini A, Rebay S, Savini M. Discontinuous Galerkin solution of the Reynolds-averaged Navier-Stokes and $k-\omega$ turbulence model equations. Computers & Fluids, Vol. 34; 2005. p. 507-540.
[11] Bassi F, Botti L, Colombo A, Crivellini A, Franchina N, Ghidoni A, et al. Very high-order accurate discontinuous Galerkin computation of transonic turbulent flows on aeronautical configurations. In: ADIGMA a European initiative on the development of adaptive higher-order variational methods for aerospace applications". Notes on numerical fluid mechanics and multidisciplinary design, Springer, Vol. 113; 2010. p.25-38.
[12] Bassi F, Rebay S. High-order accurate discontinuous Galerkin methods in computational fluid dynamics: from model problems to complex turbulent flows-Part 1 35Th CFD/Adigma Course on Very high order discretization methods, edited by H. Deconinck; 2008.
[13] Bassi F, De Bartolo C, Hartmann R, Nigro A. A discontinuous Galerkin method for inviscid low Mach number flows, Journal of Computational Physics vol. 228 issue 11 June 20; 2009. p. 3996-4011.
[14] Balay S, Buschelman K, Gropp WD, Kaushik D, Knepley MG, Curfman Mclnneses L, Smith BF, Zhang H. PETSc Web page http://www.mcs.anl.gov/ Petsc; 2001.
[15] Darmofal DL, Moinier P, Giles MB. Eigenmode analysis of boundary conditions for the one-dimensional preconditioned Euler equations. Journal of Computational Physics 2000;160:369-384.
[16] F.R. Menter. Two-equation eddy-viscosity turbulence models for engineering applications, AIAA Journal, Vol. 32-8; 1994. p. 1598-1605.